High Specific Activity during Electrochemical CO_2 Reduction through Homogeneous Deposition of Gold Nanoparticles on Gas Diffusion Electrodes

Takuya Yamada, [◊] Kazuyuki Iwase, [◊,*] Naoto Todoroki, [†] Itaru Honma [◊,*]

[◊] Institute of Multidisciplinary Research for Advanced Materials (IMRAM), Tohoku University, 2-1-1 Katahira, Aoba-ku, Sendai, Miyagi 980-8577, Japan

[†] Graduate School of Environmental Studies, Tohoku University, 6-2-2 Aramakiaza-Aoba Aoba-ku, Sendai, Miyagi 980-8579, Japan

ABSTRACT

The electrochemical CO_2 reduction reaction (CO_2RR) has attracted attention as a promising strategy for converting CO_2 into value-added products. Gas diffusion electrodes (GDEs) loaded with metallic nanoparticles as electrocatalysts are expected to efficiently reduce CO_2 due to the high specific surface area of such particles and the superior mass transport characteristics of GDEs. In the present study, GDEs loaded with homogeneous layers of sub-nanometer gold (Au) nanoparticles were fabricated using a radio frequency sputtering technique that had a low deposition rate. This allowed precise control of the catalyst loading. The Au-loaded GDEs exhibited significantly higher CO production efficiency compared with the electrodes fabricated by conventional deposition methods using dispersed Au nanoparticles. Additionally, a Au-loaded GDE having a catalytic layer thickness of 10 nm demonstrated a mass-based CO production activity of 1882 A g^{-1} at -0.85 V. This is the highest value yet reported. This work confirmed that the uniform deposition of sub-nanometer metallic particles gives enhanced catalyst utilization. The results of this research provide important insights into the design of efficient CO_2RR electrodes and highlight the potential of radio frequency sputtering to fabricate high-performance CO_2RR electrodes as an approach to realizing carbon-neutral technologies.

1. INTRODUCTION

The electrochemical CO_2 reduction reaction (CO_2RR) is gaining attention as a promising strategy for converting CO_2 into value-added products using electricity generated from renewable energy sources such as wind or solar energy.[1, 2] A major advantage of the CO_2RR is that this process allows the reduction of CO_2 under ambient conditions (i.e., room temperature and pressure) without the addition of energy derived from fossil fuels. Previous studies have shown that the CO_2RR can generate various products, including CO, formate ($HCOO^-$) and hydrocarbons (such as methane and ethylene). In addition, the hydrogen evolution reaction (HER) proceeds as a competing reaction at negative potentials where the CO_2RR proceeds.[3,4] Hence, controlling the selectivity for the CO_2RR and optimizing the rate of product generation (that is, the rate of reaction) are fundamental issue related to the potential industrialization of the CO_2RR.

Previous studies have shown that the appropriate choice of catalyst can control the selectivity for certain CO_2RR products, leading to extensive research in this area. Such prior work has suggested that both the metal elements comprising the catalyst and the coordination number of the active metal centers are important. As an example, noble metals such as gold (Au) and silver (Ag) are known to produce CO[3, 5, 6, 7] while elements such as tin (Sn) and zinc (Zn) tend to produce formate ($HCOO^-$).[8, 9] In addition, the use of nanoparticulate catalysts tends to provide active metal centers with low coordination numbers that exhibit good selectivity along with high specific surface areas, increased reaction rates and greater mass-based activities.[10]

The CO_2RR rate and current density can also be improved through the use of gas diffusion electrodes (GDEs) loaded with catalysts as working electrodes. In the case of the CO_2RR using a GDE, the reaction proceeds at the three-phase solid catalyst/liquid electrolyte/gaseous CO_2 interface, which avoids the mass transport limitations associated with

conventional two-phase (solid catalyst/liquid electrolyte) systems. As a result of this improvement, it has been reported that the CO_2RR can proceed at current densities suitable for practical applications (100-500 mA cm^{-2} and higher).[11-18]

On the basis of the above, nano-sized catalysts supported on GDEs are expected to provide excellent selectivity and mass-based activity during the CO_2RR. However, the fabrication of GDEs loaded with nano-sized catalysts presents a significant challenge, even though this approach could overcome the mass transport limitations of CO_2 and reveal the inherent activity of the catalysts. Although there have been attempts to achieve high current densities for using highly dispersed Ag metallic nanoparticles by combining polymers and nanoparticles, to the best of the authors' knowledge, the direct formation of nanoparticle layers on GDEs has not well been studied. In general, nanoparticles easily aggregate with consequent reductions in activity.[19] Therefore, nanoparticles are not readily supported in a dispersed manner.

Sputtering method is a promising approach to directly applying electrode catalysts to supports and prior work has demonstrated the direct formation of a catalyst layer on a GDE by sputtering with subsequent evaluation of CO_2RR activity.[20, 21] Although sputtering should permit precise control of the nanoparticle size and amount, in prior work, the supported catalyst particles were typically on the order of several hundred nanometers in size and catalyst layers having thicknesses in excess of 100 nm were typically formed.[22, 23] GDEs loaded with highly dispersed nanoparticulate catalysts by the sputtering method are expected to exhibit greater activity and efficiency when applied to the CO_2RR.[24-26] Even so, the fabrication of GDEs having highly dispersed catalytic nanoparticles by sputtering and subsequent improvements in CO_2RR performance have not yet been reported.

On this basis, the present work employed a radio frequency (RF) sputtering method to directly load nanoparticles as a means of obtaining greater catalytic activity. RF sputtering was

used because this technique allows the plasma density and applied energy to be carefully tuned and the slow metal deposition rate permits precise control of the amount of metal loaded onto the substrate. As such, this is a very attractive method for the fabrication of GDEs loaded with well-defined nanoparticles. Even so, the fabrication of catalyst loaded GDEs by RF sputtering with evaluation of the associated catalytic activities has not yet been established and the fabrication of catalyst loaded GDEs using direct current (DC) sputtering has predominantly been employed, as demonstrated by Table S1.[27-30] Even so, the fabrication of catalyst loaded GDEs by RF sputtering with evaluation of the associated catalytic activities has not yet been established and the fabrication of catalyst loaded GDEs using direct current (DC) sputtering has predominantly been employed, as demonstrated by Table S1. The aim of the work reported herein was to demonstrate the above-mentioned concept by employing Au as a model catalyst to generate CO, an important feedstock for the Fischer-Tropsch process, via the CO_2RR.[31, 32]

2. Experimental

2.1 Electrode fabrication

Au nanoparticle loaded GDEs (Au-GDEs) were fabricated by directly sputtering Au on GDEs (MFK-A, Mitsubishi Chemical) using a specially designed RF sputtering system. The pure Au target with a diameter of 2.5 cm and thickness of 1 mm and having 99.999% purity (PLASMATERIALS) was used for the preparation of catalyst loaded GDEs. The base pressure of the sputtering chamber was 1×10^{-7} Pa and sputtering was conducted with an RF discharge power of 40 W under argon (Ar, Taiyo Nippon Sanso, 99.9999 vol.%) at a flow rate of 25 sccm and a chamber pressure of 0.5 Pa. The sputtering rate under these conditions was estimated to be 0.40 nm s^{-1} using a quartz crystal microbalance thickness monitor (SQM160, INFICON). The Au loading on each GD was controlled by changing the sputtering duration to prepare Au-GDEs with Au layers having nominal thicknesses of 10, 50, 100, 200 or 500 nm. These electrodes are referred to herein as Au-X, where X corresponds to the aforementioned thickness.

GDEs coated with Au nanoparticles were fabricated by spraying catalyst inks onto the devices using an airbrush (Anest Iwata, Eclipse HP-BS). These electrodes are referred to herein as the Au-Spray samples. These Au nanoparticles were synthesized using a citrate reduction method based on a modification of a previously reported procedure and labeled as Au-NP in the manuscriupt.[33] Briefly, hydrogen tetrachloroaurate (III) tetrahydrate ($HAuCl_4 \cdot 4H_2O$, Wako, Guaranteed Reagent grade) was firstly dissolved in ultrapure water to a concentration of 1040 ppm and heated to boiling. Following this, 5 wt% of trisodium citrate dihydrate (Wako, Guaranteed Reagent grade) was added to the solution with continuous stirring to give a Au:citrate molar ratio of 2.5:1. Upon mixing, the solution color was observed to change from yellow to wine red, indicating the formation of Au nanoparticles. The solution was stirred for a further 3 min, followed by cooling to room temperature. The nanoparticles were subsequently recovered by centrifugation and then washed three times with ultrapure water. Finally Au-NP

was diluted with ultrapure water. The final Au concentration in the resulting dispersion of Au-NP was determined to be 1550 ppm using inductively coupled plasma atomic emission spectroscopy (ICP-AES). The catalyst inks were prepared by ultrasonication of a mixture comprising 300 μL of this Au nanoparticles dispersion, 900 μL of ethanol (Wako, Guaranteed Reagent) and 10 μL of a 5 wt% Nafion solution (Wako, polymer content: 5.0-5.4%). The catalyst loading was approximately 246 mg cm^{-2}.

2.2 Physical characterizations

Scanning electron microscopy (SEM) images and energy dispersive X-ray spectroscopy (SEM-EDX) mapping data were obtained using a JSM-7800F instrument (JEOL Ltd.). A cross-sectional polisher (IB-09020CP, JEOL Ltd.) was employed to prepare the samples prior to acquiring SEM images. Transmission electron microscopy (TEM) observations of the Au-NPs were performed with an H-7650 instrument (Hitachi). X-ray diffraction (XRD) patterns were obtained using a SmartLab3G (Rigaku Corp.) to determine the crystalline structures of the Au-GDEs and of the original Au-NPs. X-ray absorption spectroscopy (XAS) analyses were performed at the BL01B01 beamline of the SPring-8 facility operated by the Japan Synchrotron Radiation Research Institute (JASRI) in conjunction with a double-crystal Si (111) monochromator. With the exception of the Au-500, each Au-GDE was examined while operating in the fluorescent mode and employing a 19-element solid-state detector. The Au-500 and the Au-NPs were assessed using the transmission mode, with the Au-NPs having been pelletized. Data analysis was conducted using the Demeter software package.[34] The chemical composition and electronic environment of the Au, both of which can affect the catalytic properties of the material, were investigated by acquiring X-ray photoelectron spectroscopy (XPS) data using a PHI5000 VersaProbe II instrument (ULVAC Phi Corp.).

2.3 Electrochemical assessments

Electrochemical measurements were performed using an HZ-7000 potentiostat (Hokuto Denko) equipped with an HZAP3003A booster (Hokuto Denko). Custom-made electrochemical cells[35] were employed for the evaluation of CO_2RR activity. Sodium dihydrogen phosphate (NaH_2PO_4, Wako, Guaranteed Reagent), disodium hydrogen phosphate (Na_2HPO_4, Wako, Guaranteed Reagent) and potassium hydrogen carbonate ($KHCO_3$, Sigma-Aldrich, ACS reagent, 99.7%) were used to prepare the electrolyte. Each reagent was used as received without further purification. Catalyst-loaded GDEs, Ag/AgCl (in a saturated KCl solution) and carbon paper loaded with IrO_2 (Tanaka Precious Metals, TEM77100(SA100)) were employed as the working, reference and counter electrodes, respectively. The geometric surface area of each working electrode was 1.89 cm^2. The anodic and cathodic compartments were separated by a proton exchange membrane (Nafion 117, Sigma-Aldrich) and a 1 M $KHCO_3$ solution was used as the electrolyte for the evaluation of CO_2RR activity in each trial. Gaseous CO_2 (Taiyo Nippon Sanso, 99.995%) was fed to the apparatus at a flow rate of 10 sccm using a mass flow controller and the CO_2RR products were analyzed after 30 min of constant current electrolysis for evaluation of CO_2RR activity. Gas phase products were captured using a gasbag and quantitatively analyzed with a gas chromatograph (GC-2014, Shimadzu) equipped with a thermal conductivity detector to analyze H_2 and a flame ionization detector with a methanizer (MTN-1, Shimadzu) to analyze CO. Liquid products were analyzed using ^{1}H nuclear magnetic resonance spectroscopy (NMR), employing an AVANCE III 600 (Bruker). These assessments were carried out via a pre-saturation method reported elsewhere using dimethyl sulfoxide (Wako) as an internal standard.[36] Electrode potentials were converted to reversible hydrogen electrode (RHE) values and *IR* compensation was conducted based on impedance spectroscopy. Cyclic voltammetry (CV) data were acquired using a custom-made single-compartment cell with a three-electrode system. In each trial, a catalyst-loaded GDE

placed in an AE9-1 sample holder (EC Frontier, electrode area: 0.20 cm^2), Ag/AgCl (in a saturated KCl solution) and a Au wire were employed as the working, reference and counter electrodes, respectively. A 1 M $KHCO_3$ solution saturated with CO_2 or a 1 M phosphate buffer solution (PBS) saturated with Ar was used as the electrolyte. The solution pH was adjusted to 7.8 in each case. The scan rate was 50 mV s^{-1}.

3. Results and discussion

Au-GDEs were prepared via the direct sputtering of Au using an RF sputtering method. A TEM image of the Au-NPs synthesized in this work is presented in Fig. S1, indicating that the size of Au-NPs were estimated mean diameter of 24 nm. The photographic images of the Au-GDEs and Au mass loadings calculated based on the sputtering thicknesses are provided in Fig. S2.

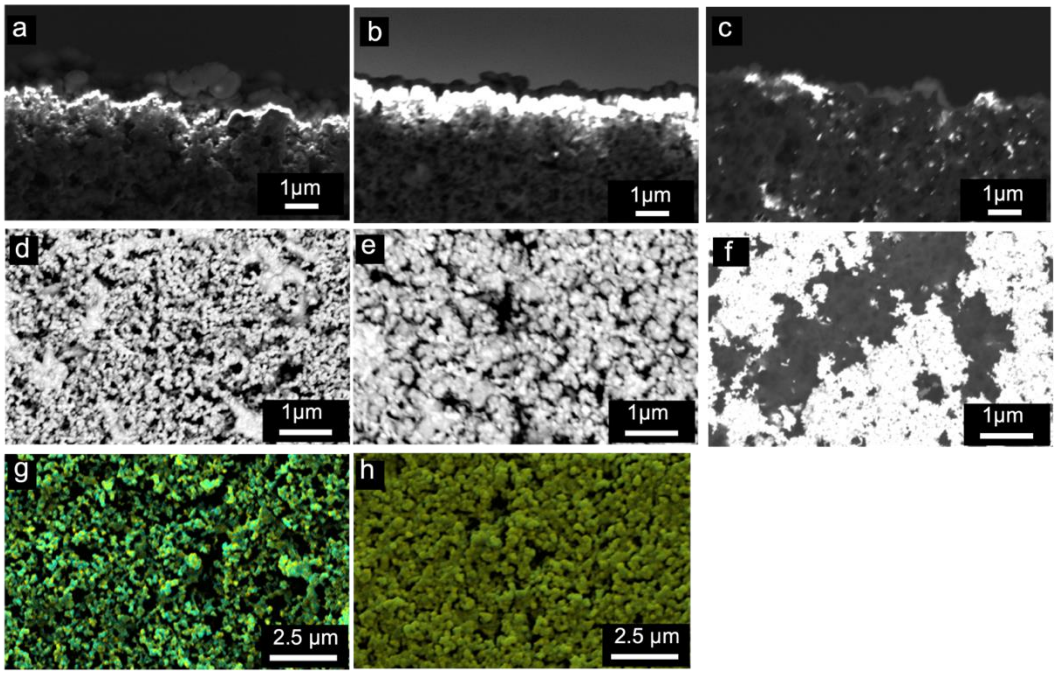

Figure 1. SEM images of the (a, d, g) Au-100, (b, e, h) Au-500, and (c, f) Au-Spray. (a-c) Cross-sectional and (d-f) overhead view of the reflected electron SEM images. In these images, the white dots represent Au and the dark gray regions indicate carbon nanoparticles on the GDEs. (g, h) SEM-EDX mapping data obtained from overhead views, in which Au and C appear as yellow and blue regions, respectively. The elemental mass-based proportions obtained from these analyses were Au:C = 36.7:55.3 and Au:C = 92.7:7.3 for the Au-100 and Au-500, respectively.

The structures of the Au-GDEs were directly characterized by microscopy and Fig. 1 shows representative SEM images acquired from the Au-100, Au-500 and Au-Spray. Catalyst

layers (CLs) composed of Au particles (shown here in white) were evidently applied homogeneously to the surfaces of microporous layers (MPLs) on the GDEs (indicated by dark gray) via the sputtering process. However, it should be noted that the GDE surfaces exhibit microscopic-scale irregularities in Figs. 1(a) and 1(b). It is also apparent that the CL thickness increased as the sputtering time was increased, suggesting that the Au loading amount could be controlled by changing the sputtering time, as was intended. Interestingly, the CL on the surface of the Au-Spray was inhomogeneous and some white dots can also be seen within the MPL (Fig. 1(c)). These results suggest the formation of an inhomogeneous CL and also indicate that the Au-NPs did not remain solely on the MPL surface but also penetrated into the interior. The SEM images of the Au-100 and Au-500 surfaces (Figs. 1(d) and 1(e)) demonstrate that the Au particles (again showing as white regions) were homogeneously distributed over the GDE surfaces, confirming that homogeneous CLs were obtained. Additionally, black areas not covered by Au-NPs can be observed on the GDEs, indicating that the original porous structures were maintained. These Au-GDEs fabricated by sputtering would therefore be expected to function as electrodes during CO_2RR. The SEM image of Au-Spray surface in Fig. 1(f) demonstrates that the white area composed of Au-NPs and the dark gray part composed of bare carbon particles on the GDE were completely separated. Hence, it appears that Au-NPs underwent aggregation during the electrode fabrication process and that some of Au-NPs go into MPLs of GDEs, as discussed above. The secondary electron SEM images presented in Fig. S3 show essentially the same results. The EDX mapping data acquired from SEM analyses of the Au-100 and Au-500 surfaces are presented in Figs. 1(g) and 1(h), respectively. In the case of Au-100, carbon (which appears blue) and Au (which appears yellow) appear to have formed a homogeneous mixture. These data suggest that Au-NPs were dispersed homogeneously over the surface whereas the MPLs were either exposed on the surface or the CLs were too thin to prevent the detection of carbon. In contrast, the surface of Au-500 is almost entirely covered in

yellow, corresponding to Au. A semiquantitative analysis based on these SEM-EDX results provided Au:C elemental ratios of 36.7:55.3 for the Au-100 and 92.7:7.3 for the Au-500, respectively. As suggested by the surface SEM images, these results indicate that the proportion of Au present in the CL increased along with the sputtering time.

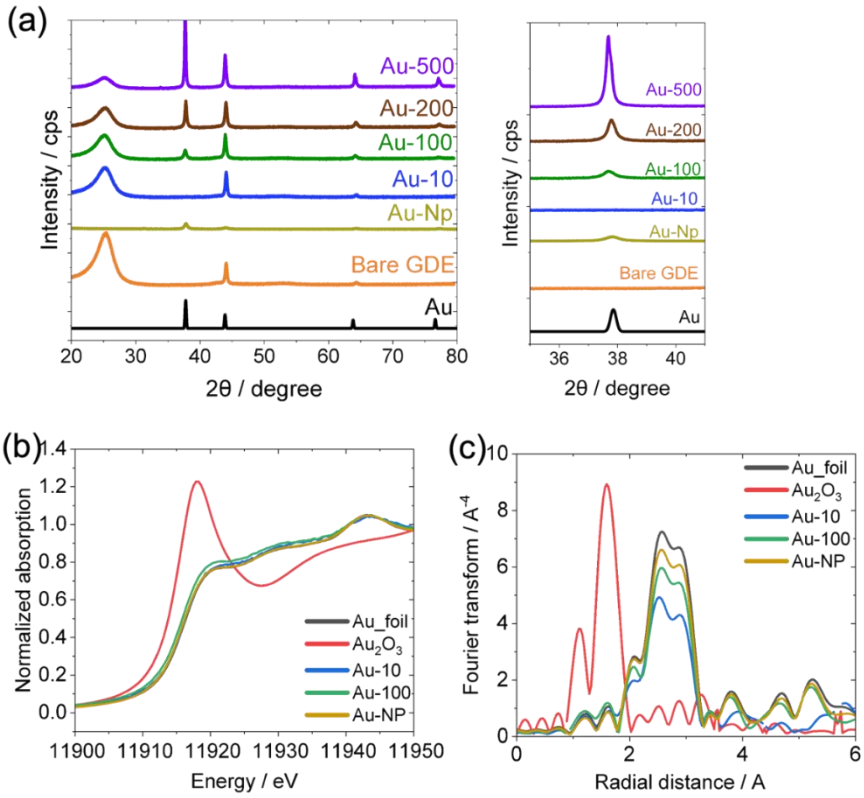

Figure 2. Physical characterizations of Au-GDEs and of the Au-NPs used for the fabrications of the Au-Spray sample. (a) XRD patterns along with the ICSD:759736 pattern for Au as a reference. (b) Au L3-edge XANES and (c) k^3-weighed EXAFS spectra. Au foil and Au_2O_3 were employed as reference materials representing metallic Au and an Au oxide. All data were analyzed using the Demeter Athena package. [34]

The XRD patterns for Au-GDEs and Au-NPs used to produce Au-Spray are provided in Fig. 2(a). Peaks corresponding to metallic Au (ICSD: 759736) appeared at 38.0°, 44.1° and 64.1° for all Au-GDEs and Au-NPs. Additionally, the intensity of the metallic Au peaks in the pattern of each of Au-GDEs fabricated by the sputtering method increased along with the Au

loading. From this result, it is apparent that the Au species in these samples were polycrystalline Au.

The valence and coordination structures of the Au in the Au-GDEs and Au-NPs were characterized by XAS analyses and the Au L3-edge XANES and Fourier transform (FT) EXAFS are shown in Figs. 2(b) and 2(c), respectively. The XANES spectra obtained from Au-10, Au-100, Au-500 and Au-NPs as well as from Au-foil and Au_2O_3 as references are presented in Fig. 2b. The Au-10, Au-100 and Au-NPs all exhibited absorption edges and XANES structures similar to those of Au-foil, suggesting that the Au in each of those samples was present as Au(0).[37, 38] The surface XPS data obtained from the Au-10 and Au-500 (Fig. S4) also indicate that the Au in the Au-10 and Au-500 was in the Au(0) state.[39, 40] The coordination structures of the Au species were confirmed by FT-EXAFS with the results shown in Fig. 2c. The coordination structures of the Au species were confirmed by FT-EXAFS with the results shown in Fig. 2(c). The Au-GDEs and the Au-NPs all provided peaks in the range of 2.6 to 2.9 Å that were assigned to Au-Au scattering with no peaks around 1.6 Å (assignable to Au-O scattering as observed in Au_2O_3). From these findings, it is evident that metallic Au particles were formed in each case, in agreement with the XRD patterns and XANES spectra. Further information regarding the coordination structures of Au in the Au-GDEs and Au-NPs was acquired by curve fitting of the FT-EXAFS. The curve fits and corresponding parameters are summarized in Table S2. The coordination numbers (CNs) estimated by curve fitting of the EXAFS results were 9.1, 9.0 and 11.4 for the Au-100, Au-10 and Au-NPs, respectively. Previous research has suggested that the CN reflects the nanoparticle size[41] and nanoparticles having a mean size of approximately 1.7 nm have been found to have a CN of 8.8.[42,43] Therefore, these result indicate that the Au-GDEs and Au-NPs had sizes in the range of 1-5 nm.

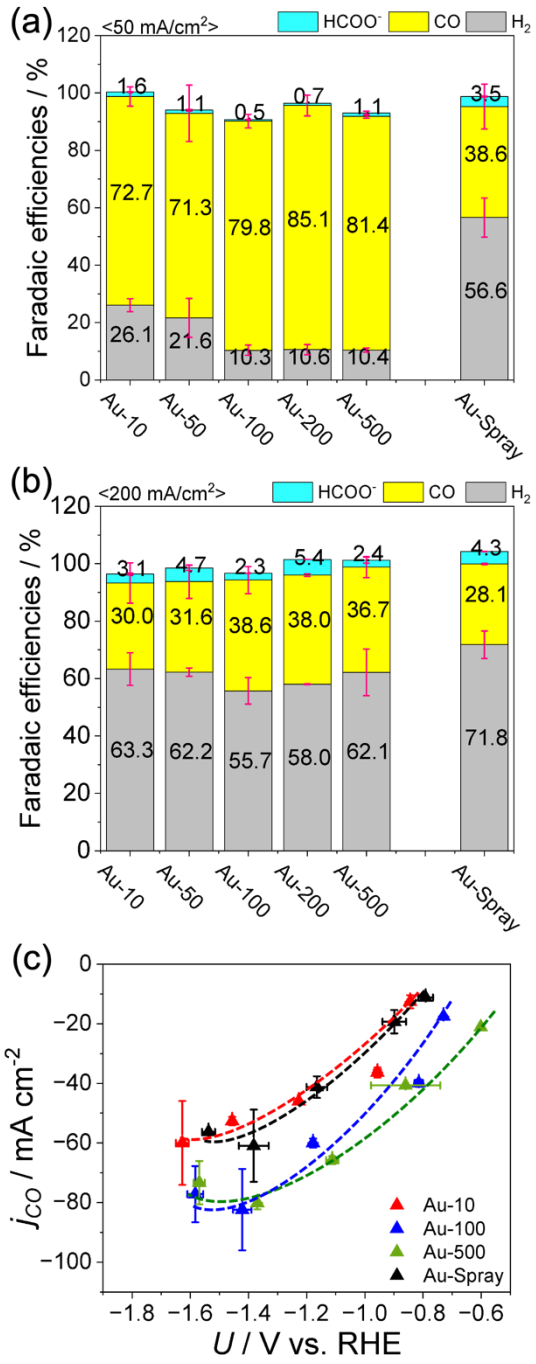

Figure 3. CO_2RR activities of Au-GDEs. FE values for various CO_2RR products as determined at current densities of (a) 50 and (b) 200 mA cm^{-2}. (c) Partial current densities for CO generation (j_{CO}) as functions of potential for the Au-10, Au-100, Au-500 and Au-Spray. The dotted lines are simply visual aids.

The electrocatalytic activities of the various Au-GDEs during the CO2RR were subsequently evaluated under neutral conditions (pH=7.8). First, cyclic voltammograms (CVs) were acquired from the Au-10, Au-200 and Au-Spray samples in 1 M PBS saturated with Ar or 1 M $KHCO_3$ saturated with CO_2 (Fig. S5). The Au-GDEs each exhibited a cathodic onset in the range of approximately −0.3 to −0.4 V versus RHE in both electrolytes, whereas a bare GDE only produced very low cathodic currents in either electrolyte. These results confirmed that the Au played an important role in terms of generating the cathodic current. While Au-200 showed an increase in current in the CO_2-saturated $KHCO_3$ solution compared with that measured in the Ar-saturated PBS, Au-100 and Au-Spray did not show any significant increase. In CO_2-saturated $KHCO_3$ solution, an oxidation current was observed in the positive potential region above 0.4 V for all Au-GDEs. This oxidation current can possibly be attributed to the re-oxidation of the formate ($HCOO^-$) or CO generated via the CO_2RR in the negative potential region. [44,45] These ions or molecules may have remained close to the electrode surface or have been adsorbed on the Au.

The CO_2RR activities of the Au-GDEs were evaluated by performing constant current experiments (galvanostatic conditions) using a two-compartment cell separated by a Nafion membrane (see Experimental section for details). Figures 3(a) and 3(b) show the Faradaic efficiencies (FEs) associated with various CO_2RR products as determined at current densities of 50 and 200 mA cm^{-2}, respectively. The CO_2RR activity evaluated under other conditions are summarized in Fig. S6. Both CO and $HCOO^-$ were detected as CO_2RR products along with H_2 as a byproduct generated by the HER, in agreement with the results of prior work using GDEs loaded with Au nanoparticles.[46] The FE values for CO production exceeded 70% for all Au-GDEs at 50 mA cm^{-2} (Fig. 5(a)) while the FE values related to the HER and to CO generation were observed to decrease and increase, respectively, as the Au loading was increased going from the Au-10 to the Au-100. However, there were no further significant changes in FE for

CO generation at loadings above that of the Au-100. The CO production efficiency obtained from the Au-Spray was 39%, which was lower than that of the Au-GDEs fabricated by the sputtering process. This lower CO efficiency can possibly be ascribed to the presence of bare carbon nanoparticles on the GDE surface as observed in the SEM images, since such bare carbon nanoparticles would tend to promote the HER rather than the CO_2RR.[47] The CO_2RR activity values observed at 200 mA cm^{-2} are summarized in Fig. 3(b). The FEs for H_2 production were increased compared with those at 50 mA cm^{-2} for all samples, with a slight increase in the FEs for $HCOO^-$ production and a decrease in the FEs for CO production. Even under these conditions, the FE values for CO generation increased as the Au loading amount was increased on going from the Au-10 to the Au-100. However, no significant increase in this value was observed at higher Au loadings, with a maximum of approximately 39%. The FE for CO production exhibited by the Au-Spray was 28.1% even at 200 mA cm^{-2}, which was still lower than that of the Au-GDEs prepared by sputtering. The evident decrease in the FEs for CO generation at higher current densities could be caused by the contribution of the carbon nanoparticles on GDEs to the electrochemical reactions, since they promote HER.[47]

Because CO was the main CO_2RR product in the present study, the effect of potential on the partial current density associated with CO generation (j_{CO}) using the Au-10, Au-100, Au-500 and Au-Spray was assessed, with the results shown in Fig. 3(c). This graph presents the data acquired at current densities of 25 and 200 mA cm^{-2}. The j_{CO} were observed at -0.85 V in the case of the Au-10 and Au-Spray up to -0.6 V for the Au-500 and beginning at approximately -0.75 V for the Au-100. When the Au loading was increased on going from the Au-10 to the Au-100, the j_{CO} values were increased in all potential regions and j_{CO} increased to approximately -80 mA cm^{-2} in the vicinity of -1.4 V in the case of the Au-100 and Au-500. These findings can be attributed to an increase in the amount of Au catalysts that promoted the CO_2RR to generate CO. Although no significant effect on the maximum j_{CO} value was observed

with increases in Au loading above that of the Au-100, j_{CO} was increased in the low overpotential region. No significant differences were observed between the Au-10 and Au-Spray. The Au loading of Au-Spray was intermediate between those of the Au-100 and Au-200 (see the Experimental section). These results show that the maximum j_{CO} of the Au-Spray (-1.4 V) was approximately 70% that of Au-100 and Au-200 prepared by sputtering, with almost the same Au loading, and almost 50% in the lower overpotential region (i.e., -0.8V). Therefore, the Au-GDEs fabricated by sputtering exhibited higher CO generating activity than Au-Spray.

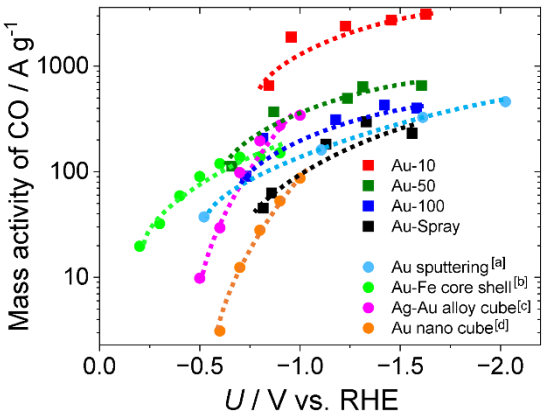

Figure 4. CO generation activities of various Au-GDEs normalized by Au mass-loading. a: Ref. [27] , b: Ref. [16], c,d: Ref. [48]. The calculated Au loading of the Au-10 and Au-100 were 19.32 and 193.2 μg cm^{-2}, respectively. The mass loadings for the sputtered samples were [a] 193.2, [b] 200, [c] 500 and [d] 500 μg cm^{-2}. The dotted lines are included simply as visual aids.

As demonstrated in Fig. 3(c), the Au-GDEs fabricated by the sputtering method all exhibited similar j_{CO} values with lower Au loadings compared with that of the Au-Spray. These results demonstrate that the Au-GDEs fabricated by the sputtering method in this study provided greater mass-based activities during CO generation (that is, higher j_{CO}/Au mass loading values). The sputtering method allowed highly dispersed Au nanoparticles to be deposited on the GDEs, as indicated by the SEM images in Fig. 1, which could account for the higher j_{CO}/Au mass values of the Au-GDEs fabricated by sputtering. To assess this possibility,

the effects of potential on the j_{CO}/Au mass loading values of the present Au-GDEs and of previously reported Au-loaded GDEs were evaluated. Figure 4 shows the j_{CO}/Au mass values determined for the Au-10, Au-100, Au-500 and Au-Spray and the values reported for Au-based catalysts deposited on GDEs.[16, 27 48] Compared with Au-spray, Au-100 provided a higher j_{CO}/Au mass loading value, as discussed above. Interestingly, Au-GDEs fabricated by sputtering in the present work also exhibited greater j_{CO}/Au mass values than have been previously reported for GDEs loaded with Au nanoparticles and even Au-loaded electrodes fabricated by sputtering in previous research. The improved performance observed in the work reported herein may have been a consequence of the highly dispersed Au nanoparticles deposited on the GDEs, as was evident from the SEM (Fig. 1) and EXAFS (Fig. 2). In addition, the j_{CO}/Au mass values increased as the Au loading was decreased. Specifically, the Au-10 showed the highest value of 1882 A g^{-1} at -0.85 V.

Here we discuss the factors responsible for the higher j_{CO}/Au mass values for the Au-GDEs fabricated by sputtering in this study. Two main reasons can be supplied, related to the particle size and to the CL structure. In the former case, the Au particles in the Au-GDEs fabricated by sputtering had sizes in the range of 1-5 nm, as determined by EXAFS and CN analyses and summarized in Fig. 2(c) and Table S1, respectively. The smaller particle size would have resulted in a higher specific surface area, leading to a greater j_{CO}/Au mass value. Another factor, related to the electrode structure, is the uniformity of the CL. As can be seen from the SEM images in Fig. 1, Au nanoparticles were uniformly deposited on the surfaces of the GDEs when using the sputtering method. In contrast, Au nanoparticles were aggregated on the GDE surfaces, leading to the formation of the inhomogeneous CL for Au-Spray. It is likely that Au-GDEs fabricated by sputtering in this study exhibited higher j_{CO}/Au mass values compared with the Au-Spray and previously-reported Au-loaded GDEs due to the effects of both of these two factors.

Finally, the stability of the Au-GDEs made by sputtering was assessed by performing long-term galvanostatic trials. Specifically, the CO_2RR activity of the Au-100 at 50 mA cm^{-2} was evaluated (Fig. S7). The main CO_2RR product was CO during this experiment and the associated FE gradually decreased while that for H_2 generation increased over the 4 h duration of the experiment. After 270 min, the total FE for both CO and H_2 production drastically decreased, likely as a consequence of electrolyte flooding as reported previously.[49, 50] Further studies intended to improve the activity and durability of the electrode by inhibiting flooding of the electrode will be conducted in the future.

4. Conclusions

Au nanoparticles loaded GDEs were fabricated using an RF sputtering method as an approach to achieving a highly efficient CO_2RR. SEM, EDX and XAS analyses showed that metallic Au nanoparticles were uniformly deposited on the GDE surfaces, which is not possible using the conventional spraying technique. CO_2RR activity assessments revealed that the Au-10, which had an especially low Au loading, exhibited the highest mass-based activity for CO formation. This performance was ascribed to the formation of a uniform CL composed of sub-nanoscale Au particles. This study suggested that RF sputtering enables the uniform deposition of Au nanoparticles on GDEs. This process permits the amount of metal that is loaded to be precisely controlled, so as to effectively fabricate efficient CO_2RR electrodes. Increasing the Au loading was also found to reduce the CO_2RR overpotential due to the associated increase in surface conductivity. The CO_2RR is one of the key reactions associated with realizing a carbon-neutral society and this study provides important insights into means of achieving large-scale, high-efficiency electrolysis.

ASSOCIATED CONTENT

Supporting Information

Cyclic voltammograms, TEM images, XPS spectra, electrochemical data, results from long-term testing of the Au-100 at 50 mA cm^{-2}, curve fitting of EXAFS data using the Artemis software.

Authors Information

Corresponding Author

Kazuyuki Iwase* - *Institute of Multidisciplinary Research for Advanced Materials (IMRAM), Tohoku University, 2-1-1 Katahira, Aoba-ku, Sendai, Miyagi, 980-8577, Japan*

E-mail : kazuyuki.iwase.a6@tohoku.ac.jp

Itaru Honma - *Institute of Multidisciplinary Research for Advanced Materials (IMRAM), Tohoku University, 2-1-1 Katahira, Aoba-ku, Sendai, Miyagi, 980-8577, Japan*

E-mail : itaru.homma.e8@tohoku.ac.jp

Authors

Takuya Yamada - *Institute of Multidisciplinary Research for Advanced Materials (IMRAM), Tohoku University, 2-1-1 Katahira, Aoba-ku, Sendai, Miyagi, 980-8577, Japan*

Naoto Todoroki - *Graduate School of Environmental Studies, Tohoku University, 6-2-2 Aramakiaza-Aoba Aoba-ku, Sendai, Miyagi 980-8579, Japan*

Notes

The authors declare no competing financial interest.

Acknowledgments

This work was supported by a KAKENHI Grant-in-Aid (no. 22H02175) from the Japan Society for the Promotion of Science (JSPS) and by a PRESTO program from the Japan Science and Technology Agency (JST) (no. JPMJPR2371). This work was also funded in part by the DOWA Seeds Development Project, a Research Grant (General Research) from the TEPCO Memorial Foundation and Ensemble grants of Tohoku University. The EXAFS analyses were conducted on the BL01B1 beamline at the Spring8 facility (proposal nos. 2022B0566, 2023A1690 and 2023A1782).

REFERENCES

(1) Masel, R. I.; Liu, Z.; Yang, H.; Kaczur, J. J.; Carrillo, D.; Ren, S.; Salvatore, D.; Berlinguette, C. P. An industrial perspective on catalysts for low-temperature CO(2) electrolysis. *Nat Nanotechnol* **2021**, *16* (2), 118-128. DOI: 10.1038/s41565-020-00823-x.
(2) Overa, S.; Ko, B. H.; Zhao, Y.; Jiao, F. Electrochemical Approaches for CO2 Conversion to Chemicals: A Journey toward Practical Applications. *Accounts of Chemical Research* **2022**, *55* (5), 638-648. DOI: 10.1021/acs.accounts.1c00674.
(3) Hori, Y.; Kikuchi, K.; Suzuki, S. Production of Co and Ch4in Electrochemical Reduction of Co2at Metal Electrodes in Aqueous Hydrogencarbonate Solution. *Chem. Lett.* **1985**, *14* (11), 1695-1698. DOI: 10.1246/cl.1985.1695.
(4) Noda, H.; Ikeda, S.; Oda, Y.; Imai, K.; Maeda, M.; Ito, K. Electrochemical Reduction of Carbon Dioxide at Various Metal Electrodes in Aqueous Potassium Hydrogen Carbonate Solution. *Bull. Chem. Soc. Jpn.* **1990**, *63* (9), 2459-2462. DOI: 10.1246/bcsj.63.2459 (acccessed 2021/01/31).
(5) Chen, H.; Wang, Z.; Cao, S.; Liu, S.; Lin, X.; Zhang, Y.; Shang, Y.; Zhu, Q.; Zhou, S.; Wei, S.; et al. Facile synthesis of an antimony-doped Cu/Cu2O catalyst with robust CO production in a broad range of potentials for CO2 electrochemical reduction. *J. Mater. Chem. A* **2021**, *9* (40), 23234-23242. DOI: 10.1039/d1ta06181j.
(6) Poon, K. C.; Wan, W. Y.; Su, H.; Sato, H. A review on recent advances in the electrochemical reduction of CO(2) to CO with nano-electrocatalysts. *RSC Adv* **2022**, *12* (35), 22703-22721. DOI: 10.1039/d2ra03341k.
(7) Wu, L.; Wu, L.; Guo, C.; Guan, Y.; Wang, H.; Lu, J. Progress in Electroreduction of CO2 to Form Various Fuels Based on Zn Catalysts. *Processes* **2023**, *11* (4). DOI: 10.3390/pr11041039.
(8) Kumar, B.; Atla, V.; Brian, J. P.; Kumari, S.; Nguyen, T. Q.; Sunkara, M.; Spurgeon, J. M. Reduced SnO2 Porous Nanowires with a High Density of Grain Boundaries as Catalysts for Efficient Electrochemical CO2 - into - HCOOH Conversion. *Angewandte Chemie International Edition* **2017**, *56* (13). DOI: 10.1002/anie.201612194.
(9) Zhang, T.; Qiu, Y.; Yao, P.; Li, X.; Zhang, H. Bi-Modified Zn Catalyst for Efficient CO2 Electrochemical Reduction to Formate. *ACS Sustainable Chemistry & Engineering* **2019**, *7* (18). DOI: 10.1021/acssuschemeng.9b01985.
(10) Mohan, A.; Jaison, A.; Lee, Y.-C. Emerging trends in mesoporous silica nanoparticle-based catalysts for CO2 utilization reactions. *Inorganic Chemistry Frontiers* **2023**, *10* (11), 3171-3194. DOI: 10.1039/d3qi00378g.
(11) Rabiee, H.; Ge, L.; Zhang, X.; Hu, S.; Li, M.; Yuan, Z. Gas diffusion electrodes (GDEs) for electrochemical reduction of carbon dioxide, carbon monoxide, and dinitrogen to value-added products: a review. *Energy & Environmental Science* **2021**, *14* (4), 1959-2008. DOI: 10.1039/d0ee03756g.
(12) Iwase, K.; Hirano, T.; Honma, I. Copper Aluminum Layered Double Hydroxides with Different Compositions and Morphologies as Electrocatalysts for the Carbon Dioxide Reduction Reaction. *ChemSusChem* **2022**, *15* (2), e202102340. DOI: 10.1002/cssc.202102340.
(13) Ge, L.; Zhang, X.; Hu, S.; Li, M.; Zhiguo, Y. Gas diffusion electrodes (GDEs) for electrochemical reduction of carbon dioxide, carbon monoxide, and dinitrogen to value-added products: a review. *Energy & Environmental Science* **2021**, *14* (4), 1959–2008. DOI: 10.1039/D0EE03756G.
(14) Inoue, A.; Harada, T.; Nakanishi, S.; Kamiya, K. Ultra-high-rate CO2 reduction reactions to multicarbon products with a current density of 1.7 A cm−2 in neutral electrolytes. *EES Catalysis* **2023**, *1* (1), 9-16. DOI: 10.1039/d2ey00035k.
(15) Zhang, J.; Luo, W.; Züttel, A. Self-supported copper-based gas diffusion electrodes for CO_2 electrochemical reduction. *Journal of Materials Chemistry A* **2019**, *7* (46), 26285–26292. DOI: 10.1039/C9TA06736A.
(16) Sun, K.; Cheng, T.; Wu, L.; Hu, Y.; Zhou, J.; Maclennan, A.; Jiang, Z.; Gao, Y.; Goddard, W. A., 3rd; Wang, Z. Ultrahigh Mass Activity for Carbon Dioxide Reduction Enabled by Gold-Iron Core-Shell Nanoparticles. *J Am Chem Soc* **2017**, *139* (44), 15608-15611. DOI: 10.1021/jacs.7b09251.
(17) Sun, M.; Cheng, J.; Yamauchi, M. Gas diffusion enhanced electrode with ultrathin superhydrophobic macropore structure for acidic CO(2) electroreduction. *Nat Commun* **2024**, *15* (1), 491. DOI: 10.1038/s41467-024-44722-4.
(18) Iwase, K.; Kojima, T.; Todoroki, N.; Honma, I. Activity switching of Sn and In species in

Heusler alloys for electrochemical CO2 reduction. *Chemical Communications* **2022**, *58* (31), 4865-4868, Article. DOI: 10.1039/d2cc00754a.
(19) Wang, R.; Haspel, H.; Pustovarenko, A.; Dikhtiarenko, A.; Russkikh, A.; Shterk, G.; Osadchii, D.; Ould-Chikh, S.; Ma, M.; Smith, W. A.; et al. Maximizing Ag Utilization in High-Rate CO2 Electrochemical Reduction with a Coordination Polymer-Mediated Gas Diffusion Electrode. *ACS Energy Letters* **2019**, *4* (8). DOI: 10.1021/acsenergylett.9b01509.
(20) Jeng, E.; Qi, Z.; Kashi, A. R.; Hunegnaw, S.; Huo, Z.; Miller, J. S.; Bayu Aji, L. B.; Ko, B. H.; Shin, H.; Ma, S.; et al. Scalable Gas Diffusion Electrode Fabrication for Electrochemical CO(2) Reduction Using Physical Vapor Deposition Methods. *ACS Appl. Mater. Interfaces* **2022**, *14* (6), 7731-7740. DOI: 10.1021/acsami.1c17860.
(21) Huq, F.; Sanjuán, I.; Baha, S.; Braun, M.; Kostka, A.; Chanda, V.; Junqueira, J. R. C.; Sikdar, N.; Ludwig, A.; Andronescu, C. Influence of the PTFE Membrane Thickness on the CO2 Electroreduction Performance of Sputtered Cu - PTFE Gas Diffusion Electrodes. *ChemElectroChem* **2022**, *9* (1). DOI: 10.1002/celc.202101279.
(22) Del Castillo, A.; Alvarez-Guerra, M.; Solla-Gullón, J.; Sáez, A.; Montiel, V.; Irabien, A. Sn nanoparticles on gas diffusion electrodes: Synthesis, characterization and use for continuous CO 2 electroreduction to formate. *Journal of CO2 Utilization* **2017**, *18*, 222-228. DOI: 10.1016/j.jcou.2017.01.021.
(23) Puring, K. J.; Siegmund, D.; Timm, J.; Möllenbruck, F.; Schemme, S.; Marschall, R.; Apfel, U.-P. Electrochemical CO2 Reduction: Tailoring Catalyst Layers in Gas Diffusion Electrodes. *Advanced Sustainable Systems* **2021**, *5* (1). DOI: 10.1002/adsu.202000088.
(24) Siegel, J.; Lyutakov, O.; Rybka, V.; Kolska, Z.; Svorcik, V. Properties of gold nanostructures sputtered on glass. *Nanoscale Res Lett* **2011**, *6* (1), 96. DOI: 10.1186/1556-276X-6-96.
(25) Cojocaru, B.; Neaţu, Ş.; Sacaliuc-Pârvulescu, E.; Lévy, F.; Pârvulescu, V. I.; Garcia, H. Influence of gold particle size on the photocatalytic activity for acetone oxidation of Au/TiO2 catalysts prepared by dc-magnetron sputtering. *Appl. Catal. B* **2011**, *107* (1-2), 140-149. DOI: 10.1016/j.apcatb.2011.07.007.
(26) Qi, Z.; Kashi, A. R.; Buckley, A. K.; Miller, J. S.; Ye, J.; Biener, M. M.; Foucher, A. C.; Stach, E. A.; Ma, S.; Kuhl, K. P.; et al. Effect of Gold Catalyst Surface Morphology on Wetting Behavior and Electrochemical CO2 Reduction Performance in a Large-Area Zero-Gap Gas Diffusion Electrolyzer. *J. Phys. Chem. C* **2022**, *126* (46). DOI: 10.1021/acs.jpcc.2c03773.
(27) Sassenburg, M.; de Rooij, R.; Nesbitt, N. T.; Kas, R.; Chandrashekar, S.; Firet, N. J.; Yang, K.; Liu, K.; Blommaert, M. A.; Kolen, M.; et al. Characterizing CO(2) Reduction Catalysts on Gas Diffusion Electrodes: Comparing Activity, Selectivity, and Stability of Transition Metal Catalysts. *ACS Appl Energy Mater* **2022**, *5* (5), 5983-5994. DOI: 10.1021/acsaem.2c00160.
(28) Woldu, A. R.; Wang, Y.; Guo, L.; Hussain, S.; Shah, A. H.; Zhang, X.; He, T. Ar-plasma activated Au film with under-coordinated facet for enhanced and sustainable CO2 reduction to CO. *Journal of CO2 Utilization* **2021**, *54*. DOI: 10.1016/j.jcou.2021.101776.
(29) Dinh, C.-T.; García de Arquer, F. P.; Sinton, D.; Sargent, E. H. High Rate, Selective, and Stable Electroreduction of CO2 to CO in Basic and Neutral Media. *ACS Energy Lett.* **2018**, *3* (11), 2835-2840. DOI: 10.1021/acsenergylett.8b01734.
(30) Monti, N. B. D.; Fontana, M.; Sacco, A.; Chiodoni, A.; Lamberti, A.; Pirri, C. F.; Zeng, J. Facile Fabrication of Ag Electrodes for CO2-to-CO Conversion with Near-Unity Selectivity and High Mass Activity. *ACS Applied Energy Materials* **2022**, *5* (12), 14779-14788. DOI: 10.1021/acsaem.2c02143.
(31) Ojeda, M.; Nabar, R.; Nilekar, A. U.; Ishikawa, A.; Mavrikakis, M.; Iglesia, E. CO activation pathways and the mechanism of Fischer–Tropsch synthesis. *Journal of Catalysis* **2010**, *272* (2), 287-297. DOI: 10.1016/j.jcat.2010.04.012.
(32) Hondo, E.; Lu, P.; Zhang, P.; Li, J.; Tsubaki, N. Direct Production of Hydrocarbons by Fischer-Tropsch Synthesis Using Newly Designed Catalysts. *Journal of the Japan Petroleum Institute* **2020**, *63* (5), 239-247. DOI: 10.1627/jpi.63.239.
(33) Ji, X.; Song, X.; Li, J.; Bai, Y.; Yang, W.; Peng, X. Size control of gold nanocrystals in citrate reduction: the third role of citrate. *J. Am. Chem. Soc.* **2007**, *129* (45), 13939-13948. DOI: 10.1021/ja074447k.
(34) Ravel, B.; Newville, M. ATHENA, ARTEMIS, HEPHAESTUS: data analysis for X-ray absorption spectroscopy using IFEFFIT. *J. Synchrotron Radiat.* **2005**, *12* (4), 537-541. DOI: 10.1107/S0909049505012719.

(35) Iwase, K.; Kamimura, T.; Honma, I. Ag-Sn Intermetallic Compounds Synthesized via Mechanical Alloying as Electrocatalysts for CO₂ Reduction Reaction. *Electrochemistry* **2024**. DOI: 10.5796/electrochemistry.24-00052.
(36) Li, C. W.; Ciston, J.; Kanan, M. W. Electroreduction of carbon monoxide to liquid fuel on oxide-derived nanocrystalline copper. *Nature* **2014**, *508* (7497), 504-507. DOI: 10.1038/nature13249.
(37) Abécassis, B.; Testard, F.; Kong, Q.; Francois, B.; Spalla, O. Influence of Monomer Feeding on a Fast Gold Nanoparticles Synthesis: Time-Resolved XANES and SAXS Experiments. *Langmuir* **2010**, *26* (17). DOI: 10.1021/la1020274.
(38) Benfield*, R. E.; Grandjean, D.; Kröll, M.; Pugin, R.; Thomas Sawitowski, a.; Schmid*, G. Structure and Bonding of Gold Metal Clusters, Colloids, and Nanowires Studied by EXAFS, XANES, and WAXS. *The Journal of Physical Chemistry B* **2001**, *105* (10). DOI: 10.1021/jp0028812.
(39) Casaletto, M. P.; Longo, A.; Martorana, A.; Prestianni, A.; Venezia, A. M. XPS study of supported gold catalysts: the role of Au0 and Au+δ species as active sites. *Surface and Interface Analysis* **2006**, *38* (4). DOI: 10.1002/sia.2180.
(40) Hepperle, P.; Herman, A.; Khanbabaee, B.; Baek, W. Y.; Nettelbeck, H.; Rabus, H. XPS Examination of the Chemical Composition of PEGMUA - Coated Gold Nanoparticles. *Particle & Particle Systems Characterization* **2022**, *39* (9). DOI: 10.1002/ppsc.202200070.
(41) Miyanaga, T.; Nakamae, M.; Nago, H.; Ohori, Y.; Fujikawa, T. Photoelectron Mean Free Path on the EXAFS Analyses for Nanoparticles. *e-Journal of Surface Science and Nanotechnology* **2012**, *10* (0), 565-568. DOI: 10.1380/ejssnt.2012.565.
(42) Duan, Z.; Li, Y.; Timoshenko, J.; Chill, S. T.; Anderson, R. M.; Yancey, D. F.; Frenkel, A. I.; Crooks, R. M.; Henkelman, G. A combined theoretical and experimental EXAFS study of the structure and dynamics of Au147 nanoparticles. *Catal. Sci. Technol.* **2016**, *6* (18), 6879-6885. DOI: 10.1039/c6cy00559d.
(43) Chill, S. T.; Anderson, R. M.; Yancey, D. F.; Frenkel, A. I.; Crooks, R. M.; Henkelman, G. Probing the Limits of Conventional Extended X-ray Absorption Fine Structure Analysis Using Thiolated Gold Nanoparticles. *ACS Nano* **2015**, *9* (4), 4036-4042. DOI: 10.1021/acsnano.5b00090.
(44) Marcandalli, G.; Villalba, M.; Koper, M. T. M. The Importance of Acid-Base Equilibria in Bicarbonate Electrolytes for CO(2) Electrochemical Reduction and CO Reoxidation Studied on Au(hkl) Electrodes. *Langmuir* **2021**, *37* (18), 5707-5716. DOI: 10.1021/acs.langmuir.1c00703.
(45) Wei, Z.; Zhang, M. K.; Zhu, B. Q.; Cai, J.; Chen, Y.-X. Mechanistic Insight into Formic Acid/Formate Oxidation at the Au(111) Electrode: Implications from the pH Effect and H/D Kinetic Isotope Effect. *J. Phys. Chem. C* **2022**, *126* (29), 11987-12002. DOI: 10.1021/acs.jpcc.2c03029.
(46) Alinejad, S.; Quinson, J.; Wiberg, G. K. H.; Schlegel, N.; Zhang, D.; Li, Y.; Reichenberger, S.; Barcikowski, S.; Arenz, M. Electrochemical Reduction of CO2 on Au Electrocatalysts in a Zero - Gap, Half - Cell Gas Diffusion Electrode Setup: a Systematic Performance Evaluation and Comparison to an H - cell Setup**. *ChemElectroChem* **2022**, *9* (12). DOI: 10.1002/celc.202200341.
(47) Yang, K.; Kas, R.; Smith, W. A.; Burdyny, T. Role of the Carbon-Based Gas Diffusion Layer on Flooding in a Gas Diffusion Electrode Cell for Electrochemical CO2 Reduction. *ACS Energy Lett.* **2020**, *6* (1), 33-40. DOI: 10.1021/acsenergylett.0c02184.
(48) Park, J. W.; Choi, W.; Noh, J.; Park, W.; Gu, G. H.; Park, J.; Jung, Y.; Song, H. Bimetallic Gold-Silver Nanostructures Drive Low Overpotentials for Electrochemical Carbon Dioxide Reduction. *ACS Appl. Mater. Interfaces* **2022**, *14* (5), 6604-6614. DOI: 10.1021/acsami.1c20852.
(49) De Gregorio, G. L.; Burdyny, T.; Loiudice, A.; Iyengar, P.; Smith, W. A.; Buonsanti, R. Facet-Dependent Selectivity of Cu Catalysts in Electrochemical CO(2) Reduction at Commercially Viable Current Densities. *ACS Catal* **2020**, *10* (9), 4854-4862. DOI: 10.1021/acscatal.0c00297.
(50) Dinh, C.-T.; Burdyny, T.; Kibria, M. G.; Seifitokaldani, A.; Gabardo, C. M.; Arquer, F. P. G. d.; Kiani, A.; Edwards, J. P.; Luna, P. D.; Bushuyev, O. S.; et al. CO2 electroreduction to ethylene via hydroxide-mediated copper catalysis at an abrupt interface. *Science* **2018**, *360* (6390). DOI: 10.1126/science.aas9100.